Quantification of the fine-scale distribution of Mn-nodules: insights from AUV multi-beam and optical imagery data fusion

Evangelos Alevizos[1], Timm Schoening[1], Kevin Koeser[1], Mirjam Snellen[2,3], Jens Greinert[1]

[1] GEOMAR Helmholtz Center for Ocean Research, 24148 Kiel, Germany

[2] Acoustics Group, Faculty of Aerospace Engineering, Delft University of Technology, Kluyverweg 1, 2629 HS Delft, the Netherlands

[3] Deltares, Princetonlaan 6, 3584 CB Utrecht, the Netherlands

Abstract. Autonomous underwater vehicles (AUVs) offer unique possibilities for exploring the deep seafloor in high resolution over large areas. We highlight the results from AUV-based multibeam echosounder (MBES) bathymetry / backscatter and digital optical imagery from the DISCOL area acquired during research cruise SO242 in 2015. AUV bathymetry reveals a morphologically complex seafloor with rough terrain in seamount areas and low-relief variations in sedimentary abyssal plains which are covered in Mn-nodules. Backscatter provides valuable information about the seafloor type and particularly about the influence of Mn-nodules on the response of the transmitted acoustic signal. Primarily, Mn-nodule abundances were determined by means of automated nodule detection on AUV seafloor imagery and nodule metrics such as nodules m^{-2} were calculated automatically for each image allowing further spatial analysis within GIS in conjunction with the acoustic data. AUV-based backscatter was clustered using both raw data and corrected backscatter mosaics.

In total, two unsupervised methods and one machine learning approach were utilized for backscatter classification and Mn-nodule predictive mapping. Bayesian statistical analysis was applied to the raw backscatter values resulting in six acoustic classes. In addition, Iterative Self-Organizing Data Analysis (ISODATA) clustering was applied to the backscatter mosaic and its statistics (mean, mode, 10th, and 90th quantiles) suggesting an optimum of six clusters as well. Part of the nodule metrics data was combined with bathymetry, bathymetric derivatives and backscatter statistics for predictive mapping of the Mn-nodule density using a Random Forest classifier. Results indicate that acoustic classes, predictions from Random Forest model and image-based nodule metrics show very similar spatial distribution patterns with acoustic classes hence capturing most of the fine-scale Mn-nodule variability. Backscatter classes reflect areas with homogeneous nodule density. A strong influence of mean backscatter, fine scale BPI and concavity of the bathymetry on nodule prediction is seen. These observations imply that nodule densities are generally affected by local micro-bathymetry in a way that is not yet fully understood. However, it can be concluded that the spatial occurrence of Mn-covered areas can be sufficiently analysed by means of acoustic classification and multivariate predictive mapping allowing to determine the spatial nodule density in a much more robust way than previously possible.

41
1. Introduction

1.1 Mn-nodules exploration

Research on Mn-nodules received increased attention in the last decade due to increasing prices for ores rich in Cu, Ni or Co, i.e. metal resources that are contained in Mn-nodules. In nature, the largest Mn-nodule occurrences are found in the deep sea, e.g. the equatorial Pacific between the Clarion and Clipperton fracture zone (CCZ), the Peru Basin as well as the Atlantic and Indian Ocean (Petersen et al., 2016). In the typically muddy sediments of the deep sea, Mn-nodules form an important hard substrate providing a habitat for deep sea sessile fauna such as sponges, corals and associated organisms (Vanreussel et al., 2016; Purser et al., 2016). Therefore, mapping Mn-nodule fields is a two-fold task, comprising not only the assessment of Mn-nodules and their density distribution for accurate resource assessment, but also the improved understanding of the natural habitat heterogeneity and its relation to the deep sea ecology. Knowledge about Mn-nodule habitats will support mitigation strategies for mining-induced impacts. Since an increasing number of countries move forward with exploitation plans for Mn-nodules in the CCZ, strategies for a detailed mapping of the deep sea Mn-nodule fields might become mandatory in order to proceed with licensing procedures prior to any mining activity.

Deep sea mining will cause substantial disturbances of the deep sea ecosystem since Mn-nodules, the primary hard substrate, will be removed and massive re-sedimentation of the top 20 to 30cm of sediment of the mined area will occur (Bluhm et al., 1995, Vanreussel et al., 2016).Thus, efforts have been made to investigate the effects of potential mining disturbances in the past (e.g. Thiel et al., 2001) and currently during the project "Ecological Aspects of Deep Sea Mining" as part of the Joint Programming Initiative Healthy and Productive Seas and Oceans (JPI Oceans). To study in detail the potential effects of a deep sea disturbance by Mn-nodule mining to benthic fauna, a plough-experiment was performed in 1989 in the Peru Basin as part of the DISturbance and reCOLonization project (DISCOL, www.discol.de). A plough of 8m width was towed 78 times over a 2nmi wide circular area (February-March 1989) to generate dense and less dense impact sub-areas. Photographic surveys, sediment and biological sampling before and after the disturbance (September 1989, March 1992, February 1996), showed that the plough marks were well visible even after 26 years and that the benthic fauna did not recover to its initial state. The data used in this study were collected during the SO242-1 cruise to the DISCOL area during summer 2015, 26 years after the DSICOL experiment.

1.2 The DISCOL study area

The DISCOL working area is situated 560 nmi SW of Guayaquil on the Pacific Oceanic Plate in the Peru Basin (Fig. 1A) in about 4150 m water depth. The larger DISCOL area ranges from 3800m to 4300m water depth (Fig. 1B) and is characterized by N-S oriented graben and horst structures with a deep N-S elongated basin with water depths down to 4300m. An 11 km wide seamount complex in the NE along with a second seamount complex to the SW and three

83 higher mounds to the NW clearly show that the DISCOL area is not located on a flat and
84 homogenous deep seafloor.
85   The ploughed DISCOL Experimental Area (DEA) itself is located on a relatively smooth,
86 slightly elevated part of the seafloor with a central valley of about 20m depth that dips
87 southward (Fig. 2A). When inspecting the bathymetry data generated by the autonomous
88 underwater vehicle (AUV) in more detail, the central part of the area shows a 20m deep valley,
89 the floor of which is comprised by low-relief N-S trending ridges giving the impression of a
90 braided river system (Fig. 2A). Despite the rich morphological features in the study area, it
91 does not contain steep slopes and represents a rather smooth seafloor (<5 degrees).
92
93

94 **1.3 Acoustic mapping of Mn-nodules and study objectives**

95   Acoustic mapping has proved to be a useful tool for supporting deep sea mineral
96 resource assessments. The initial studies mentioned below, showed promising results for Mn-
97 nodule detection and quantification, however, progress in more detailed and meaningful
98 method development and data processing capabilities has remained slow, mainly due to
99 fluctuations in the global interest of deep sea mining. The majority of surveys performed for
100 Mn-nodule mapping purposes rely on acoustic remote sensing and near-bottom photography
101 (de Moustier, 1985). The applicability of acoustic methods is based on the clear acoustic
102 contrast of at least 11 dB between the background deep sea soft sediment and the nodules (de
103 Moustier 1985). Weydert (1985) found that the nodule size is proportional to the average
104 backscatter strength for low frequency signals (<30 kHz). In addition, Weydert (1990)
105 concluded that it is possible to map the percentage of seafloor covered by nodules based on
106 backscatter measurements of sonar frequencies higher than 30 kHz , whereas for a frequency
107 of 9 kHz it is possible to use the backscatter response to determine whether the nodule
108 diameter is greater than 6 cm or smaller than 4 cm. Masson and Scanlon (1993) suggested that
109 lower sonar frequencies produce a much weaker acoustic contrast between nodules and
110 surrounding sediments for nodules of given size. They concluded that on a seafloor covered
111 with mixed-size nodules larger nodules will have a greater impact on the backscattered energy
112 than smaller ones. They also suggested that minor differences of nodule coverage will have a
113 considerable effect in backscatter values. A more recent study by Chakrabotry et al. (1996)
114 suggested that the nodule coverage is proportional to the backscatter strength and that for
115 low frequency (15 kHz; wavelength ca. 10 cm) the main type of scattering is Rayleigh scattering
116 (wavelength/10 < nodule size) for nodules and coherent scattering for fine sediments.
117 During one of the first deep sea studies for acoustic mapping of Mn-nodules, de Moustier
118 (1985) utilized a multi-beam echo-sounder (MBES) sonar combined with near-bottom acoustic
119 measurements and photographs from a deep towed camera system to infer nodule coverage.
120 He managed to obtain high agreement between relative backscatter intensity classes and
121 three types of nodule coverage as interpreted from seafloor imagery (dense, intermediate and
122 bare). At that time, his results highlighted the great potential of MBES technology in deep sea
123 mineral prospecting. In more recent years Lee and Kim (2004) utilized side-scan sonar (SSS) to
124 examine the relation of regional nodule abundance with geomorphology. According to their

125 qualitative analysis, lower backscatter values are related with abyssal troughs whereas
126 increased backscatter values are related to abyssal hills. Additionally, Ko et al. (2006)
127 attempted to examine the relation between MBES bathymetry and slope with nodule density
128 in the equatorial Pacific without identifying a solid pattern. Most recently, Okazaki and Tsune
129 (2013) utilized AUV-based MBES, SSS and image data for Mn-nodule abundance assessment
130 and its relation to deep sea micro-topography.
131 More recent projects regarding resource assessment of Mn-nodules at large scales (0.1' by 0.1'
132 grid cell size) have been based on various spatial modelling and decision making techniques
133 (ISA, 2010). Most commonly, the kriging method has been applied on sparse ground truth data
134 (obtained by physical box-corer sampling) while logistic regression and fuzzy logic algorithms
135 were applied in multivariate data sets of Mn-nodule-related environmental variables such as
136 sediment type, sea surface chlorophyll and Ca Compensation Depth (CCD) (Agterberg &
137 Bohnam-Carter, 1999, Carranza & Hale, 2001).
138 In this study we analyse AUV-based MBES and image data for quantitative mapping of Mn-
139 nodule densities in the Peru Basin. Particularly, we utilize local ground-truth information (Mn-
140 nodule measurements from AUV photographs) in order to investigate a) its relation to acoustic
141 classification maps and b) its potential use for predictive mapping of Mn-nodules in wider
142 areas where only hydro-acoustic information is available. Therefore, we apply two
143 unsupervised methods (Bayesian probability and ISODATA) for seafloor acoustic classification
144 and a machine learning algorithm (Random Forest) for Mn-nodule density predictions beyond
145 the areas that were optically imaged using the AUV.
146 By applying different algorithms for unsupervised classification, we aim at comparing their
147 results against quantitative ground truth data of nodule metrics from automated analyses on
148 AUV imagery. This way, we will assess the ability of classification methods in discriminating
149 areas with distinct nodule densities. To our knowledge, this is the first time the Random Forest
150 algorithm is applied for predictive mapping of Mn-nodule densities. Therefore, we examine its
151 performance and the influence of various AUV MBES data on the Mn-nodule prediction
152 results.
153
154
155 **2. Methodology**

156 **2.1 AUV MBES data acquisition and processing**

157 The data in this study were collected using the AUV "Abyss" (built by HYDROID Inc.) from
158 GEOMAR, during cruise SO242-1 where various AUV missions were flown. The AUV is
159 equipped with a RESON Seabat 7125 MBES sensor with 200 kHz operating frequency, 256
160 beams with 1 by 2 degree opening angle along and across track, respectively. From the original
161 PDS2000 sonar data, files backscatter snippet data were extracted into s7k format whereas
162 bathymetry data were extracted into GSF format. Prior to exporting, MBES bathymetric data
163 were filtered within the PDS2000 software. Bathymetry data from different AUV dive-missions
164 were jointly used for interpolating one single grid of bathymetry and backscatter (Fig.2).
165 Latency and roll-related artefacts affected bathymetry in places due to a none-constant time
166 delay for roll values creating uncorrectable artefacts in the resulting grid. Therefore, the

bathymetry was smoothed by applying a Gaussian filter with a 10 m x 10 m rectangular window with 3 and 5 standard deviations as smoothing factors in SAGA GIS. Filtered bathymetry was visually inspected for artefacts using the hill-shade function in SAGA GIS, giving satisfactory results. Vertical differences between the smoothed grid with the originally processed surface were everywhere less than 1 m, highlighting that the filtering did not cause significant smoothing and removal of finer details. The filtered bathymetric grid was used for calculating a variety of derivatives listed in Table 2.

The MBES backscatter data were processed in two ways. First, the s7k/GSF pairs were automatically corrected (for radiometric and geometric bias) and mosaicked in QPS FMGT (Fig. 2B). In addition, backscatter mosaic statistics were calculated and exported as GEOTIF files using a 10 m x 10 m neighbourhood. The raw snippets data were exported prior to any processing using a combination of in-house conversion software and QPS DMagic for merging beam data with ray-traced easting and northing. The raw snippets data were transformed from 16-bit amplitude units to dB using the formula in Eq. (1):

Backscatter (dB) = $20*\log_{10}(\text{amplitude})$ (1)

Raw backscatter data were processed by applying the Bayesian approach on certain beams as described in Alevizos et al. (2015 and 2017) whereas the gridded data were analysed with Random Forest (RF) regression trees and ISODATA clustering (see section below). An overview of the software used to process and classify each type of dataset is presented in Table 1.

2.2 Seafloor imagery and automated image analysis

AUV surveys were undertaken for collecting close-up images from the seafloor using a camera system recently described by Kwasnitschka et al (2016). In this system the camera is mounted behind a dome port along with a 15mm fish-eye lens that produces extreme wide-angle images. This type of lens and dome port configuration induces significant distortions to the image which need to be corrected prior to any image analysis processing. Surveying at altitudes of 4-8m above the seafloor and using the novel state-of the-art LED flash system, the AUV collected several hundred-thousand seafloor images at a 1Hz interval. The respective AUV surveys were designed to cover a large part of the study area with a single-track dive pattern and also to focus on two selected areas running track lines 5m apart for dense 2D image mosaicking (Fig. 2A). Each image was individually georeferenced using the AUV navigation and altitude data. This way, each pixel of the AUV imagery is translated to an actual portion of the seafloor.

For the automated image analyses (e.g. Mn-nodule counting), all images were smoothed by a Gaussian filter to remove noise and then converted to grayscale for computational speedup. Following, the images were corrected for inconsistent illumination due to the varying AUV altitude using the fSpice method described by Schoening, et al. (2012). The central (sharpest, best illuminated) region of each image was cropped and thresholded by an automatically

210 tuned intensity limit before contours in the resulting binary images were detected and fused to
211 blobs of pixels that served as nodule candidates. Each nodule candidate was finally fitted with
212 an ellipsoid to account for potentially buried parts of the nodule. The sizes of these ellipsoids
213 constitute the nodule size distribution within one image from which descriptive parameters
214 were derived. This kind of automated image processing resulted in quantitative information
215 such as: image area (square meters), number of nodules (n), percentage of seafloor covered by
216 nodules (amount of nodule pixels divided by total amount of image pixels), and the threshold
217 sizes (estimated 2D surface) of 1, 25, 50, 75 and 99 percent quantiles of the nodule size
218 distribution (comparable to a particle size analysis). A detailed publication on the nodule
219 delineation algorithm can be found in Schoenning et al. (2017), while the source code is
220 available online as Open Source (https://doi.pangaea.de/10.1594/PANGAEA.875070)
221 In this study, we considered the number of Mn-nodules per square meter as a normalized
222 measure of nodule density in order to avoid overestimation of Mn-nodules due to multiple-
223 detections between overlapping images. This metric is derived from the ratio of the number of
224 nodules detected to the area (m^2) of the image footprint (the size of the central 'good' part of
225 the image). Therefore the results of the predictive mapping are presented with 6 m x 6 m
226 resolution which is representative for the majority of image footprint sizes.
227
228

229 **2.3 Seafloor classification and prediction methods**
230
231 Three different approaches were applied for a predictive Mn-nodule mapping. The first
232 approach is an unsupervised method based on Bayesian statistics applied on raw snippet data.
233 It examines the within-beam backscatter variability in the entire area in order to estimate the
234 optimum number of seafloor classes. The output acoustic classes can then be validated with
235 available ground-truth data. The second approach, is based on the ISODATA algorithm (an
236 unsupervised method as well), applied on gridded backscatter data. This algorithm can
237 automatically adapt the number of classes to the data for given minimum and maximum
238 values set by the user. Finally, a supervised machine learning method was applied on gridded
239 bathymetric and backscatter data. This method requires a training set in order to model the
240 complex relationship between the Mn-nodules occurrences and the bathymetry, bathymetric
241 derivatives and backscatter information. The algorithm outputs a prediction grid for Mn-
242 nodule densities and also estimates the importance of each input variable in accurately
243 predicting Mn-nodule densities.
244
245
246
247
248
249
250

Hardware

	AUV RESON 7125		DeepSurveyCam (Kwasnitschka et al., 2016)
Software	**MBES bathymetry**	**MBES backscatter (snippets)**	**Imagery**
Processing	PDS2000 (sonar data), SAGA GIS (xyz, grids), ArcMap (grids)	Matlab (raw data), Fledermaus FMGT (corrected BS and mosaicking)	in-house software, ArcGIS
Classification / prediction	Random Forests (MGET)	Bayesian (raw data), ISODATA, Random Forests Mosaic and statistics	Random Forests (MGET)

251
252   **Table 1**: Datasets and methods applied in this study.
253
254
255
256

257 **2.3.1 Bayesian probability on beam backscatter**
258
259   The raw backscatter data were classified by applying the Bayesian methodology
260 developed and implemented by Simons and Snellen (2009) and Amiri-Simkooei (2009) and
261 applied by Alevizos et al. (2015). In order to enhance the method's performance, strong
262 outliers in the raw data were filtered by using a variance threshold set to 100 (i.e. 10 standard
263 deviations). Thus, beams with a snippet data variance greater than 100 were disregarded from
264 the classification process. The remaining snippet data were averaged for each beam for
265 obtaining the mean relative backscatter intensity. The Bayesian method is based on the central
266 limit theorem and the assumption that acoustic backscatter measurements of a homogeneous
267 seafloor type would express normal distribution when derived from a certain incidence angle.
268 Therefore all backscatter values were grouped per beam angle and their histograms were
269 examined separately. At first, a number of Gaussian curves were fitted to each histogram and
270 the goodness of fit was assessed by the χ^2 criterion. The minimum number of Gaussian curves
271 that fitted well the overall distribution pattern of the histogram values (i.e.: χ^2 is less than 2),
272 was considered as the optimum number of classes. Not all beam angles provided the same
273 number of Gaussian curves; therefore it was important to identify those beam angles that gave
274 consistent results about the number of classes. Usually the mid-range incidence angles
275 provided the most consistent results (Alevizos et al., 2015) regarding the Gaussian fitting;
276 hence beams from this range were utilized as reference in order to derive the optimum
277 number of classes. Once the reference beams were identified, the mean and standard
278 deviations of each Gaussian curve were used as conditions for classifying the backscatter
279 values for the rest of the beams.
280   The Bayesian technique does not require the MBES to be calibrated and allows for class
281 assignment per beam, thus maximizing the spatial resolution of the final map. The most
282 important aspects of the Bayesian technique are the internal cluster validation based on χ^2

283 criterion and the increased geo-acoustic resolution, allowing for maximal acoustic
284 discrimination of similar seafloor types (Alevizos et al., 2015).
285
286

2.3.2 ISODATA classification for grids
287
288
289 The ISODATA classification was applied to the backscatter mosaic and its derived
290 statistics (Table 2) using the ISODATA algorithm implemented in SAGA GIS. ISODATA stands for
291 Iterative Self-Organizing Data Analysis and has been applied in several marine mapping studies
292 involving backscatter information (Diaz, 1999; Hühnerbach et al., 2008; Blondel and Gomez-
293 Sichi 2009). The fundamentals of ISODATA processing are described in detail by Dunn (1977)
294 and Memarsadeghi et al. (2007). A particular advantage of this method apart from its fast
295 execution is that it estimates a suitable number of classes by dividing clusters with large
296 standard deviations and by merging similar clusters at the same time (Diaz 1999). This is done
297 automatically and the user only defines an empirical minimum and maximum number of
298 classes.
299

2.3.3 Random Forest predictive mapping for grids
300
301
302 To exploit the full range of MBES gridded data and for comparison purposes, supervised
303 classification was applied to the bathymetry, bathymetric derivatives and backscatter statistics
304 (Table 2). Applying a machine learning algorithm was encouraged due to the abundant ground-
305 truth data (nodule metrics from automated image analysis) and the high resolution of the
306 various MBES layers. The Random Forest algorithm as implemented in the MGET toolbox for
307 ArcGIS was used (http://mgel2011-kvm.env.duke.edu/mget). Initially developed by Breiman
308 (2001) it has shown good results in marine predictive habitat mapping (Stephens and Diesing
309 2014, Lucieer et al., 2013, Che-Hasan et al., 2014). The algorithm requires a training data set
310 with the response variable (here: nodule density from AUV imagery analysis results) and a set
311 of explanatory variables (here: bathymetry, bathymetric derivatives, backscatter) as inputs in
312 order to model the relationship between them. The training set provides the required
313 "knowledge" about the response variable and its corresponding explanatory variable's values.
314 At the next stage, an ensemble procedure based on several regression trees of random subsets
315 of the explanatory variables is iteratively applied for classifying/predicting Mn-nodule density
316 per grid-cell using a-priori information from the training sample. The prediction at a certain
317 grid-cell is defined by the majority votes of all random subsets of trees (Gislason et al., 2006).
318 During the iterative processing, the Random Forest will reserve randomly selected parts of the
319 training sample for internal cross-validation of the results (out-of-bag sample). During each
320 iteration, one explanatory variable is neglected and its importance score is calculated
321 according to its contribution to the resulting prediction error. The variable importance
322 calculation is considered one of the main advantages of the Random Forest algorithm. An
323 important step prior to Random Forest application is data exploration. With data exploration it
324 is possible to identify which explanatory variables are capable to discriminate patterns of

nodule density in the study area better. A standard approach is to explore the probability
density function of the response variable with each of the other gridded variables (e.g. slope,
BPI, etc.). These plots give first indications about the distribution type of the response variable
for a given explanatory variable.

The explanatory variables presented in Table 2 were chosen as good descriptors of nodule
density in the area based on the probability density functions of arbitrarily chosen classes of
nodule density (Fig. 3, Appendix). The arbitrary classes where based on the quantiles method
for classifying the nodule density histogram. It has to be noted that the arbitrary classes were
used only for data exploration and not for the prediction of nodule densities. All descriptor-
grids were resampled to 6 m x 6 m pixels in order to be compatible with the average effective
area of the AUV images upon which nodule metrics were computed.

An appropriate selection of training samples is fundamental for modelling the relationship
between the response variable and the gridded descriptor data. Particularly, the training
samples need to span the entire range of the study area capturing most of the data variability.
They have to contain as diverse values as possible regarding both the nodule density and the
corresponding gridded descriptor data.

Explanatory variables	Description
From bathymetry	**Scale: 6 m cell size**
Depth	AUV MBES, smoothed with Gaussian filter (5σ)
Slope	ArcGIS slope algorithm in percent units
BPI	Relative position of pixels compared to their neighbors. Inner radius 10m, outer radius 100 m (Iwashahi and Pike, 2007) SAGA GIS terrain analysis toolbox
LS factor	The integrated slope length and inclination, formula from Moore et al. (1991), SAGA GIS terrain analysis toolbox
Terrain Ruggedness Index (TRI)	Measure of the irregularity of a surface in 5m radius neighborhood (Iwashahi and Pike, 2007), SAGA GIS terrain analysis toolbox
Concavity	Measure of negative curvature of a surface (Iwashahi and Pike, 2007), SAGA GIS terrain analysis toolbox
From backscatter	**Scale: 10x10 m neighborhood, 6 m cell size**
mean	Average dB value of pixels falling within the neighborhood (FMGT module)
mode	Most frequent dB value of pixels falling within the neighborhood (FMGT module)
10% quantile	Value of neighborhood pixels describing the lower 10% of the total dB distribution (FMGT module)
90% quantile	Value of neighborhood pixels describing the 90% of

	the total dB distribution (FMGT module)

Table 2: Description of MBES features (bathymetric derivatives and backscatter statistics) that are used as explanatory variables in random forests predictions.

3. Results

3.1 Automated nodule detection from AUV images

The automated nodule detection algorithm results for nodule density (number of nodules m^{-2}) are shown in Fig. 4. The dense point cloud offers a detailed view of the nodule spatial distribution which can significantly enhance the interpretation of nodule density in conjunction with MBES bathymetry. In Fig. 4 the nodule density fluctuates in a pattern of alternating bands. By colorizing the seafloor surface and the bathymetric profile cross-section according to nodule density values, it can be seen that higher nodule densities appear on smooth slope features where the seafloor appears locally concave or terraced and also on the foot of these slopes which appear relatively lower compared to the surrounding area. By colouring the AUV bathymetry according to the nodule density it became clear that MBES derivatives may be useful for quantifying the nodule distribution in the entire study area. We thus calculated bathymetric derivatives such as BPI, concavity, slope and slope-related derivatives (LS factor, TRI) to be included in predicting nodule densities.

3.2 Bayesian acoustic classification of raw BS data

The Bayesian method identified six classes based on the analysis of beams with incidence angles between 38 and 42 degrees (Table 3). Despite the variance-based filtering, it was not possible to compensate for the remaining effects on beam incidence angles in the middle range and towards the nadir. We believe that these effects are responsible for the stripe-like classification at the outer part of the swath. The selection of six classes resulted from the agreement between two adjacent beams (Table 3) and the relative lower overlap of the Gaussian curves. The finally derived classes are ordinal; meaning that from class 1 to class 6 there is an increase in backscatter intensity. The spatial distribution of the acoustic classes expresses a gradient of high to low backscatter classes in the N-S direction (Fig. 5A). The nodule-free areas holding lowest backscatter values are captured clearly.

Acoustic class	PORT: (38° & 40°) central value (dB)	STARBOARD: (40° & 42°) central value (dB)
1	-60.7	-61.2
2	-59.4	-59.7
3	-57.4	-58.1

4	-56.3	-56.3
5	-54.8	-54.8
6	-52.8	-52.7

Table 3: Averaged central dB values of the Gaussians derived from reference beam angles on both sides of the AUV MBES

3.3 ISODATA applied to BS data

The ISODATA algorithm was applied to the mean, mode, 10% and 90% quantiles of the backscatter mosaic. These datasets are considered more suitable than the raw backscatter data, as they hold a more realistic representation of backscatter spatial variability and they are slightly correlated (correlation coefficients: 0.5-0.9) with the mean backscatter. The ISODATA algorithm was set to produce an optimal number of clusters for different ranges of cluster amounts (minimum number of clusters from 2 to 5; maximum number of clusters from 6 to 10). The results for all possible pairs regarding the minimum and maximum clusters were divided, indicating five or six clusters as optimal. To have comparable results with the Bayesian method, six clusters were selected for further analyses. Although the algorithm does not output classes with ordering, the ISODATA classes were reclassified based on their nodule statistics to be comparable with Bayesian results (see discussion section). The classes show a decreasing amount of nodules from north to south with the nodule-free areas being sufficiently demarcated.

3.4 Random Forest predictions using bathymetry derivatives and BS data

The RF was performed in two steps: the training and the prediction step. First a sensitivity test was carried out using different percentages of training samples (Fig. 6B) and fitting models with 200 and 1000 trees. This test is essential for examining the optimal settings prior to applying a predictive model. It also helps in quantifying the stability of results (given the random character of the process) by running the model with optimal settings repeatedly. For quantifying the model accuracy we used the percentage of variance explained by the out-of-bag samples (RF algorithm output report) whereas for assessing the prediction results, calculation of R^2 was applied for measuring the correlation between the predicted and measured nodule density. According to the sensitivity analysis, a training set with 30% of the total amount of images with Mn-nodule statistics was sufficient to explain more than 70% of the variance of the out-of-bag sub-sample when training 200 trees. It was also found that this accuracy value is not improving significantly when increasing the training sample size (Fig. 6B). By maintaining the same amount of training samples (30% of the total images acquired, ca. 2700 images) while using ten different parts of the data as training sample (ten-fold cross-

419 validation), the model performance was relatively consistent (69-72%) regarding the out-of-
420 bag variance explained (Table 4). These results refer to the Mn-nodules m^{-2} analyses. In
421 addition we tested the predictability of the 2D size of nodules using the 50% and 75%
422 quantiles of 2D sizes in square centimetres. The resulting out-of-bag variance explained was
423 found to be much lower (35-40%), independently from the number of trees and the size of the
424 training sample set. By using the results from the ten-fold cross-validation (or sensitivity test)
425 we extracted the mean importance score of each bathymetry and backscatter parameter (Fig
426 6C). Considering the prediction of Mn-nodules m^{-2}, the mean backscatter data was found to be
427 the most influencing variable which constantly scored first, followed by the BPI, bathymetry
428 and concavity. After the sensitivity test an optimal model using 30% of all images as training
429 data and growing 200 trees (1000 trees did not produce better results) was developed using
430 the explanatory variables for prediction of nodule densities. The final results of the RF method
431 express a gradient from higher to lower nodule densities from North to South (Fig. 6A). An
432 independent subsample of nodule measurements was used for validating the prediction
433 results. This validation sample consists of measurements selected at least six meters away
434 from any training location, to avoid the introduction of autocorrelation effects on the
435 validation process which could overestimate the performance of the model. The value of 6m
436 was selected as the majority of images cover a 6 m x 6 m area on the seafloor. A comparison
437 between the image-based Mn-nodule measurements and the averaged predicted values based
438 on ten different RF runs show a good average correlation based on the R^2 coefficient (Table 4).
439 This implies that there is a correlation between Mn-nodule density and MBES data, although
440 there is some degree of uncertainty that remains in the prediction model (see Appendix).
441
442
443

Training set size: 30% (ca. 2700 images) Trees: 200		
Model run#	OOB variance explained%	Predicted/Measured correlation (R^2)
1	72.5	0.69
2	73.0	0.69
3	70.6	0.68
4	70.2	0.70
5	72.2	0.70
6	72.6	0.71
7	69.3	0.69
8	71.1	0.71
9	72.9	0.68
10	70.6	0.71
average	71.5	0.7

444 Table 4: RF model performance for minimum optimal settings of training sample and number of trees
445 regarding prediction of Mn-nodule densities.
446
447 **4. Discussion**

12

448

449 Our results show that AUV imagery is capable to provide detailed information about Mn-
450 nodule densities hence assisting quantitative mapping of the Mn-nodule distribution on the
451 seafloor. Consistency and repeatability of quantitative methods are fundamental factors in
452 mapping studies and therefore automated image analysis is crucial in this regard. Expert
453 assessments of several tens of thousands of images are practically not possible in a reasonable
454 time frame and include a high rate of subjectivity. Thus, automated analysis of imagery is
455 regarded as a very suitable method for quantitative mapping of Mn-nodules. This however
456 comes at the cost that usually AUV image surveys are spatially restricted due to the low
457 altitude above the seafloor. For larger scale quantitative mapping of nodule fields, AUV
458 imagery data need to get spatially linked with AUV hydro-acoustic data supporting with data
459 from all regions of interest at the seafloor. Results from image analysis can then be used as
460 alternative information for acoustic class validation and predictive mapping. Although image
461 analysis results do not constitute ground-truth information they are the best available data to
462 correlate with acoustic classification and prediction results. By exploring the relationship
463 between Mn-nodule data with bathymetry, bathymetric derivatives and acoustic backscatter,
464 we aim to identify potential linkages that allow extrapolation of nodule information to larger
465 areas to assess mineral resources, determine benthic habitats or learn about geological
466 processes that might influence nodule growth. The following paragraphs discuss the
467 performance of the applied classification and prediction methods highlighting the potential
468 use of high resolution Mn-nodule density maps by considering various sources of errors
469 induced throughout the data analyses.

470
471

472 **4.1 Fine scale spatial variability of Mn-nodule density**

473

474 Both, the unsupervised classifications (ISODATA, Bayesian) and the random forest prediction
475 results are largely comparable to the nodule detection measurements map (Fig. 7). Hence,
476 both classification and prediction data, and nodule measurements reflect a similar spatial
477 distribution pattern of nodule densities. The Mn-nodule densities seen in the imagery highlight
478 a pattern of alternating high and low density bands on bathymetric slope features. According
479 to studies on the fine scale (tens of meters) distribution of Mn-nodules as summarized by
480 Margolis and Burns (1976) higher nodule densities are related to hilltops, slopes and the foot
481 of slopes. The authors particularly highlighted that e.g. nodule sizes vary significantly over
482 short distances; unfortunately there were no methods to capture this variability sufficiently at
483 the time of this study. The correlation to the bathymetry is supported by the variable
484 importance plot of the RF model (Fig. 6C). This plot shows that both bathymetry and
485 backscatter features contribute significantly to the prediction of the Mn-nodule densities with
486 variables such as mean backscatter intensity, fine scale BPI, and concavity as good predictors.
487 The predictive potential of these variables needs to be validated in future studies using MBES
488 data from different study areas.

489

Both unsupervised acoustic classes and the Random Forest prediction suggest a gradient of decreasing nodule densities from north to south while the RF quantitative map (Fig. 6A) shows more gradual changes regarding the fine-scale spatial distribution of Mn-nodules. The northern part of the MBES survey is located very close to, and partly within, a seamount area. According to towed camera video footage these seamounts comprise ancient volcanoes that are now covered with deep sea fine sediments. In addition, a few pillow-basalt outcrops were found along with basalt slabs being exposed on the seamount slopes. Greater nodule densities can be observed from these images suggesting that accumulated nodules or exposed basalt rocks may be assigned to the same acoustic class that represents higher acoustic intensities. In the random forest prediction, high nodule densities could be confused with basalt rock as well (Fig. 6A, black arrows). Video data can be used in order to differentiate these seafloor types in the acoustic classes. Greater nodule densities in the vicinity of the seamounts area can be explained by the findings presented by Vineesh et al. (2009) and Sharma et al., (2013). These two studies propose that in the proximity of abyssal hills and slopes, abundant basalt fragments act as nodule nuclei that favour nodule development. Away from the seamount area, the nodule density variations follow a banded pattern of high and low density alternations with localized depressions representing nodule-free areas (Fig. 2B). The band-pattern variation is not fully understood by the datasets available in this study; however, it is assumed that it is the result of a combination of the deep sea benthic boundary layer hydrodynamics, local sediment movement and active tectonics that impacts pore fluid migration. It is not clear why and how the nodule-free areas are formed and why we observe moderate nodule densities in broad deep plains of the area. Margolis and Burns (1977) suggest that bathymetric valleys are more influenced by sedimentation hence not favouring nodule growth, but that hill tops and bathymetric slopes are covered by a greater amount of nodules due to a lower impact of local sedimentation. Whether this explanation is also true for the described study area remains speculative. In any case, backscatter data clearly indicate where areas of higher and lower Mn-nodule densities exist, allowing for future investigations of the underlying factors.

4.2 Assessing the Mn-nodule acoustic classification

To assess the performance of unsupervised classification methods in clustering homogeneous areas of Mn-nodules, we examined the within- and between-class variability of the Mn-nodules densities (nodules m^{-2}). The assessment is based on the descriptive statistics of nodule measurements from each class (Table 5) and box-plots of nodules m^{-2} from each class (Fig. 8). The box-plots assist to better illustrate the separation between classes as well.
To evaluate the separation of Mn-nodule densities that fall within different acoustic classes (Bayesian and ISODATA), we performed a Welch ANOVA along with a Games-Howell test for testing whether the mean values between the classes differ significantly. This test was selected, because the Levene's test (Martin & Bridgmon, 2012) indicated that there is no homogeneity between the class variances for both classification methods ($p \ll 0.05$).

Particularly the results of the Welch ANOVA for nodule populations belonging to the same Bayesian class ($F(5,905)=700$, $p=<<0.05$) and ISODATA ($F(5, 2520)=810$, $p<<0.05$) support the finding that the mean values of Mn-nodules densities differ significantly between the different classes. This finding supports that classification results effectively resolve acoustically homogenous areas of nodule patches which are statistically distinct to each other.

Regarding the Bayesian classification results, the ordinal type of the classes can be noticed both in the statistics and the box-plots (Table 5, Fig. 8A). The mean and median values of nodules m^{-2} are increasing with increasing class number suggesting that higher backscatter values are related to higher nodule densities. Class 1 represents the lowest nodule densities but without including samples of zero nodules, this would make this class more distinguishable with an even lower mean value. Some class overlap can be observed in the box-plot for the Bayesian classes; the within-class standard deviation is increasing with acoustic class number, suggesting larger ambiguity for areas with increased nodule density. Classes resulted from the ISODATA clustering hold similar standard deviations suggesting a similar degree of within-class variability. Overall, Mn-nodule density classes express high within-class variability with almost 50% of within-class measurements spanning in a wider range of values causing class overlap (Fig. 8). This can be attributed to few factors such as inaccurate navigation between the different AUV deployments, shortcomings of the image-based nodule detection algorithm and noise in the backscatter data (see Appendix). However, it can be inferred from the box-plots for each unsupervised method that seafloor areas of homogeneous Mn-nodule density can be discriminated by classifying the MBES backscatter information only.

No useful results were obtained for the 2D size of nodules (in cm^2) when examining their descriptive statistics and box-plots with acoustic classes. This might be explained by limited interfering between acoustic wavelength and the nodules radii. The high frequency (200 kHz) MBES signal results in ca. 8 mm pulse-wavelength for 1500 $m\ s^{-1}$ sound speed in seawater. This wavelength is significantly shorter than the average nodule size in the study area (>3 cm) suggesting that the dominant backscattering is sensitive to nodule density and not to nodule size. Early acoustic studies on Mn-nodules were based on low frequency sonars; therefore there is little or no information about the acoustic backscatter of nodules at high MBES frequencies (> 100 kHz). However, results from this study are in agreement with findings of Weydert (1985) according to which, frequencies higher than 30 kHz are more suitable for mapping the nodule density than the nodule size. This can be attributed to the fact that high frequency signals are more susceptible to surface roughness which is caused by fluctuating nodule densities. Therefore it is suggested that backscatter would increase with increased nodule density given that seafloor roughness increases as more nodules occur per seafloor area.

Bayes – Mn-nodules m^{-2}					
Class	samples	mean	median	mode	St.dev.
1	91	1.4	0.7	0.4	1.4
2	1760	1.7	0.9	0.9	1.9
3	2200	3.6	3.6	3.6	2.4
4	2347	4.6	4.5	4.6	2.7
5	1500	5.5	5.1	4.9	3.4
6	756	7.5	7.3	6.4	3.6
ISODATA – Mn-nodules m^{-2}					
Class	samples	mean	median	mode	St.dev.
1	3468	2.2	1.4	0	2.3
2	2732	3.5	3.5	2.9	2.3
3	2800	4.8	4.7	4.7	2.4
4	570	5.9	6.1	4.9	3.2
5	628	7.0	6.9	5.2	3.6
6	964	7.7	7.3	6.6	3.6

577
578 **Table 5**: Descriptive statistics highlighting the within-class variability of Mn-nodules for both
579 classification methods.
580
581
582

583 **4.3 Implications of acoustic mapping on Mn-nodule resource assessment and benthic habitat**
584 **characterization**
585

586 Obtaining high resolution seafloor acoustic classes and quantitative spatial predictions of the
587 Mn-nodule density provides useful information for deep sea mining and impact management.
588 The obvious application is a more realistic resource assessment (total tonnage of Mn-nodules
589 per area) which can assist a better delineation of particular areas with mining interest on large
590 and small scales. Resource assessment can be based on semi-quantitative information
591 provided by acoustic classes that correspond to particular Mn-nodule densities or quantitative
592 results from the RF predictive map.
593

594 In addition, quantitative maps of Mn-nodule densities can be used to support extrapolations of
595 benthic biota densities to seafloor areas where benthic information is not available. This is
596 possible by considering the nodule substrate as surrogate for habitat mapping of certain biota.
597 Surrogacy for mapping deep sea ecosystems has been incorporated in the study of Anderson
598 et al. (2011); the authors point out, that geomorphic classes can be used for discriminating
599 habitats in broad scales of tens to hundreds of kilometres. They also highlight that any
600 surrogacy approach should be based on the correlation between the physical variables (e.g.
601 bathymetry, backscatter) and the biological patterns that appear in the study area. In
602 Vanreussel et al. (2016) and Amon et al. (2016) it is shown that seafloor covered with more
603 Mn-nodules features higher epifaunal densities. This relation might be further evaluated to

604 have a better and verified relationship between nodule and biota densities allowing estimating
605 biota abundances in larger areas that have only been mapped acoustically.
606
607
608 **5. Conclusions**
609
610 AUV-based optical and acoustic mapping at high spatial resolution opens up new opportunities
611 for mapping Mn-nodule fields. In this study, automated image analysis provided dense,
612 quantitative information about Mn-nodules at fine scale. This information offers useful insights
613 about the fine scale variability of Mn-nodule densities while it can be utilized for correlations
614 with seafloor acoustic classes and predictive mapping. It was found that the Mn-nodule
615 density within a 500 m x 500 m photo mosaic varies in a pattern of alternating bands (with
616 denser and sparser amounts of nodules) according with smooth bathymetric slopes with a
617 preference of increased nodule occurrence at concave seafloor morphologies. Areas with
618 different nodule densities produced distinct backscatter classes that distinguished nodule
619 populations with distinct mean density values. This suggests that Mn-nodule densities can be
620 efficiently mapped with high resolution hydro-acoustic data. In addition, applying machine
621 learning methodology showed great potential in quantitative predictive mapping of Mn-
622 nodules through modelling the complex relation between image-derived nodule metrics with
623 bathymetric derivatives and backscatter statistics. In essence, by using a relatively small
624 amount of AUV images (ca. 2700) as the training set it was possible to obtain a 70% correlation
625 between predicted and measured Mn-nodule densities. High quality and spatial resolution
626 AUV hydro-acoustic and optical data can provide a fast and less costly mean for Mn-nodule
627 mapping. This has three major implications in deep sea studies: 1) it raises questions about
628 what causes the Mn-nodules to follow the fine scale bathymetric morphology, 2) it assists in
629 better resource assessment of Mn-nodules and provides the information needed for planning
630 the optimal mining path and 3) it provides more accurate information about Mn-nodule
631 substrate as a benthic habitat, hence it can be utilized for better understanding the deep sea
632 ecology and ecological impact of potential Mn-nodule mining.
633
634
635
636

References

646 **References**

647
648
649 Agterberg, F. P., and Bonham-Carter, G.F.: ,Logistic regression and weights of evidence modeling in
650   mineral exploration, Proc. 28th Interna. Symp. Computer Applications in the Mineral Industries,
651   Golden, Colorado, 483-490,1999.
652 Alevizos, E., Snellen, M., Simons, D.G., Siemes, K., and Greinert, J.,: Acoustic discrimination of relatively
653   homogeneous fine sediments using Bayesian classification on MBES data. Mar Geol, 370, 31–42.
654   doi:10.1016/j.margeo.2015.10.007, ISSN 0025-3227, 2015.
655 Amiri-Simkooei, A.R., Snellen, and M., Simons, D.G.,: River bed sediment classification using MBES
656   backscatter data, Journal of the Acoustic Society of America,126, 1724–1738,2009.
657 Amon, D. J., Ziegler, A. F., Dahlgren, T. G., Glover, A. G., Goineau, A., Gooday, A. J., Wiklund, H.,and
658   Smith, C. R.: First insights into the abundance and diversity of abyssal megafauna in a
659   polymetallic-nodule region in the eastern Clarion-Clipperton Zone,Sci Rep 6:30492.
660   doi:10.1038/srep30492, 2016
661 Anderson, T.J., Nichol, S.L., Syms, C., Przeslawski, and Harris, P.T.,: Deep-sea bio-physical variables as
662   surrogates for biological assemblages, an example from the Lord Howe Rise, Deep Sea Research
663   Part II: Topical Studies in Oceanography, 58, 979-991,2011.
664 Blondel, P. and Gomez Sichi,O.,: Textural analyses of multibeam sonar imagery from Stanton Banks,
665   Northern Ireland continental shelf. Applied Acoustics, 70, 1288–1297,2009.
666 Bluhm, H. : Monitoring megabenthic communities in abyssal manganese nodule sites of the East
667   Pacific Ocean in association with commercial deep-sea mining. Aquatic Conservation, Marine
668   and Freshwater Ecosystems 4, 187–201, 1994
669 Breiman, L.,: RandomForests.Mach.Learn.45,5–32, 2001.
670 Carranza, E. J. M., and Hale, M.,: Geologically constrained fuzzy mapping of gold mineralization
671   potential, Baguio district, Philippines, Natural Resources Research 10, 125-136, 2001.
672 Chakraborty, B., Pathak, D., Sudhakar, M. and Raju, Y. S.: Determination of Nodule Coverage Parameters
673   Using Multibeam Normal Incidence Echo Characteristics: A Study in the Indian Ocean, Marine
674   Georesources and Geotechnology, 15, 33–48.,doi: 10.1080/10641199709379933,1996.
675 Che Hasan, R., Ierodiaconou, D., Laurenson, L., and Schimel, A.,: Integrating multibeam backscatter
676   angular response, mosaic and bathymetry data for benthic habitat mapping. PLoS ONE,
677   doi:10.1371/journal.pone.0097339,2014.
678 de Moustier, C.: Inference of manganese nodule coverage from Seabeam acoustic backscattering data.
679   Geophysics, 50, 989–1005,1985.
680 Díaz, J. V. M.,: Analysis of Multibeam Sonar Data for the Characterization of Seafloor Habitats, MEng
681   Thesis, University of New Brunswick, pp. 153,1999.
682 Dunn, J. C.,: A Fuzzy Relative of the ISODATA Process and Its Use in Detecting Compact Well-Separated
683   Clusters". Journal of Cybernetics., 3, 32-57, 1973.
684 Gislason, P.O., Benediktsson, J.A., and Sveinsson J.R.,: Random Forests for land cover classification,
685   Pattern Recognition Letters, Volume 27, Issue 4, 294-300, ISSN 0167-8655,
686   http://dx.doi.org/10.1016/j.patrec.2005.08.011, 2006.

687 Hühnerbach, V., Blondel, Ph., Huvenne, V., and Freiwald, A.,: Habitat mapping on a deepwater coral reef
688   off Norway, with a comparison of visual and computerassisted sonar imagery interpretation. In:
689   Todd B, Greene G, editors. Habitat mapping. Geological association of Canada special paper, vol.
690   47. 297–308, 2008.
691 ISA (2010). A Geological Model of Polymetallic Nodule Deposits in the Clarion-Clipperton Fracture
692   Zone. Technical Study: No. 6, International Seabed Authority, Kingston, Jamaica.
693   http://www.isa.org.jm/files/documents/EN/Pubs/GeoMod-web.pdf
694 Iwahashi, J., and Pike, R.J.,: Automated classifications of topography from DEMs by an unsupervised
695   nested-means algorithm and a three-part geometric signature. Geomorphology, 86, 409–440,
696   2007.
697 Ko, Y., Lee, S., Kim, J., Kim, K.,H., and Jung, M.,S.,: Relationship between Mn nodule abundance and
698   other geological factors in the northeastern Pacific: application of GIS and probability method,
699   Ocean Sci. J. 41(3),149-161,2006.
700 Kwasnitschka, T., Köser, K., Sticklus, J., Rothenbeck, M., Weiß, T., Wenzlaff, E., Schoening, T., Triebe,
701   L., Steinführer, A., Devey, C., and Greinert, J., : DeepSurveyCam—A Deep Ocean Optical
702   Mapping System, Sensors 16 (2),164,2016
703 Lee, S.,H., and Kim, K.H.,: Side-scan sonar characteristics and manganese nodule abundance in the
704   Clarion-Clipperton Fracture Zones NE equatorial Pacific, Mar. Georesour. Geotech, 22, 103-114,
705   2004.
706 Lucieer, V., Hill, N.A., Barrett, N.S., and Nichol S.: Do marine substrates 'look' and 'sound' the same?
707   Supervised classification of multibeam acoustic data using autonomous underwater vehicle
708   images. Estuarine Coastal Shelf Sci.117, 94–106,,2013.
709 Margolis, S. V., and Burns, R. G.,: Pacific deep-sea manganese nodules: their distribution, composition
710   and origin. Annual Review of Earth and Planetary Sciences, 4, 229-263,1976.
711 Martin, W. E., and Bridgmon, K. D.,: Quantitative and statistical research methods: from hypothesis to
712   results. New Jersey: John Wiley & Sons, ISBN: 978-0-470-63182-9,2012.
713 Masson,D. G., and Scanlon, K. M.: Fe-Mn Nodule Field Indicated GIoria, North of the Puerto Rico
714   Trench, Geo-Marine Letters, 208-213,1992.
715 Memarsadeghi, N., Mount, D.M., Netanyahu, N.S., and Moigne, J.L.: A fast implementation of the
716   isodata clustering algorithm. International Journal of Computational Geometry and Applications
717   17, 71–103, 2007.
718 Moore, I.D., Grayson, R.B., and Ladson, A.R.,: Digital terrain modelling: a review of hydrological,
719   geomorphological, and biological applications. Hydrological Processes, 5, 3 – 30, 1991.
720 Okazaki, M., and Tsune, A.,: Exploration of Polymetallic Nodules Using AUV in the Central Equatorial
721   Pacific, Proc. of the ISOPE Ocean Mining Symposium, Szczecin, Poland, 22-26 September 2013,
722   32-38,2013.
723 Petersen, S., Krätschell, A., Augustin, N., Jamieson, J., Hein, J. R. and Hannington, M. D.: News from the
724   seabed – Geological characteristics and resource potential of deep-sea mineral resources,
725   Marine Policy, 70 , pp. 175-187. DOI 10.1016/j.marpol.2016.03.012, 2016
726 Purser, A., Marcon, Y., Hoving, H.J.T., Vecchione, M., Piatkowski, U., Eason, D., Bluhm, H., and Boetius,
727   A.,: Association of deep-sea incirrate octopods with manganese crusts and nodule fields in the

728   Pacific Ocean, Current Biology, 26, Issue 24, 2016, R1268-R1269, ISSN 0960-9822,

729   http://dx.doi.org/10.1016/j.cub.2016.10.052,2016

730   Roberts, J.J., Best, B.D., Dunn, D.C., Treml, E.A., and Halpin, P.N.,: Marine Geospatial Ecology Tools: An

731   integrated framework for ecological geoprocessing with ArcGIS, Python, R, MATLAB, and C++.

732   Environmental Modelling & Software, 25, 1197-1207. doi: 10.1016/j.envsoft.2010.03.029, 2010.

733   Schoening, T., Kuhn, T., and Nattkemper, T.W.,: Estimation of poly-metallic nodule coverage in benthic

734   images, Proc. of the 41st Conference of the Underwater Mining Institute (UMI),2012.

735   Sharma, R., Khadge, N.H., and Sankar, S.J.,: Assessing the distribution and abundance of seabed

736   minerals from seafloor photographic data in the Central Indian Ocean Basin, International journal

737   of remote sensing, 34 (5), 1691-1706,2013.

738   Simons, D.G., and Snellen, M.,: A Bayesian technique to seafloor classification using multi-beam echo-

739   sounder backscatter data. Applied Acoustics, 70, 1258-

740   1268,http://dx.doi.org/10.1016/j.apacoust.2008.07.013, 2009.

741   Stephens, D., and Diesing, M.,: A Comparison of Supervised Classification Methods for the Prediction

742   of Substrate Type Using Multibeam Acoustic and Legacy Grain-Size Data. PLoS ONE,

743   doi:10.1371/journal.pone.0093950, 2014.

744   Thiel, H.,: Evaluation of the environmental consequences of polymetallic nodule mining based on the

745   results of the TUSCH Research Association, Deep Sea Research Part II: Topical Studies in

746   Oceanography, 48, (17–18),3433-3452. doi: http://dx.doi.org/10.1016/S0967-0645(01)00051-0,

747   2001

748   Vanreusel, A., Hilario, A., Ribeiro, P. A., Menot, L., and Arbizu, P. M.: Threatened by mining, polymetallic

749   nodules are required to preserve abyssal epifauna. Sci. Rep. 6:26808. doi:

750   10.1038/srep26808,2016

751   Vineesh, T. C., Nath, B. N., Banerjee, R., Jaisankar, S. and Lekshmi, V. : Manganese Nodule Morphology

752   as Indicators for Oceanic Processes in the Central Indian Basin, International Geology Review, 51,

753   27–44,2009.

754   Weydert, M.,: Measurements of the acoustic backscatter of selected areas of the deep seafloor and

755   some implications for the assessment of manganese nodule resources, J Acoustical Society of

756   America, 88, 350–366,1990.

757   Weydert, M.,: Measurement of acoustic backscattering of the deep seafloor using a deeply towed

758   vehicle. A technique to investigate the physical and geological properties of the deep seafloor

759   and to assess manganese nodule resources, Ph.D thesis, San Diego: University of California, 1985.
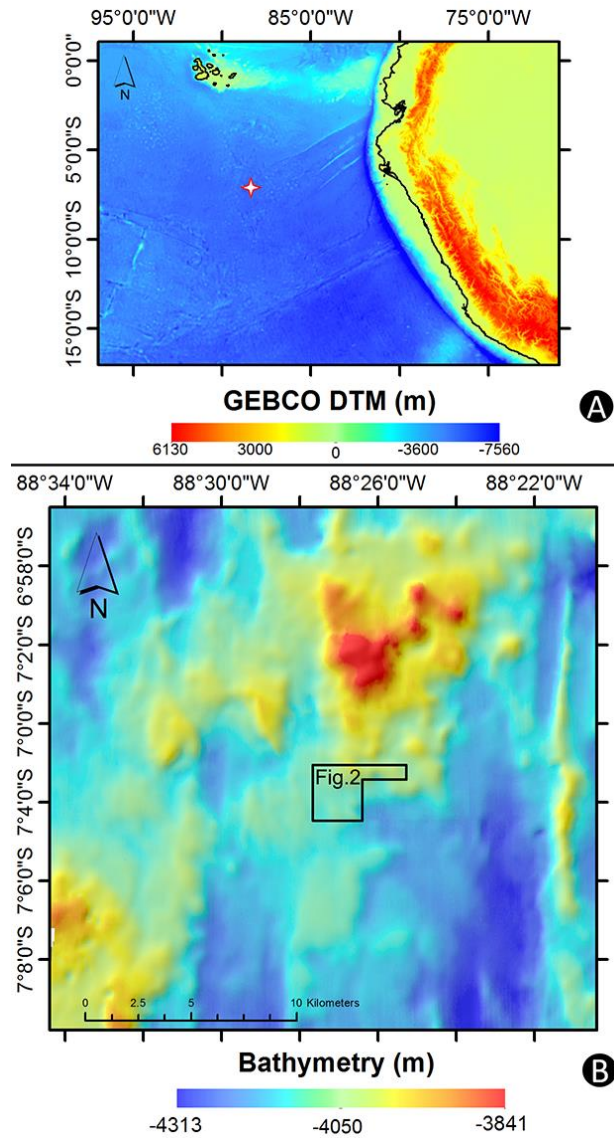
Fig. 1: A) The DISCOL area location in the Peru Basin (red star). B) Ship-based, shaded bathymetry of the wider DISCOL area with 40 m pixel size. The black rectangle represents the boundaries of the AUV MBES dataset used in this study (Fig.2).

762
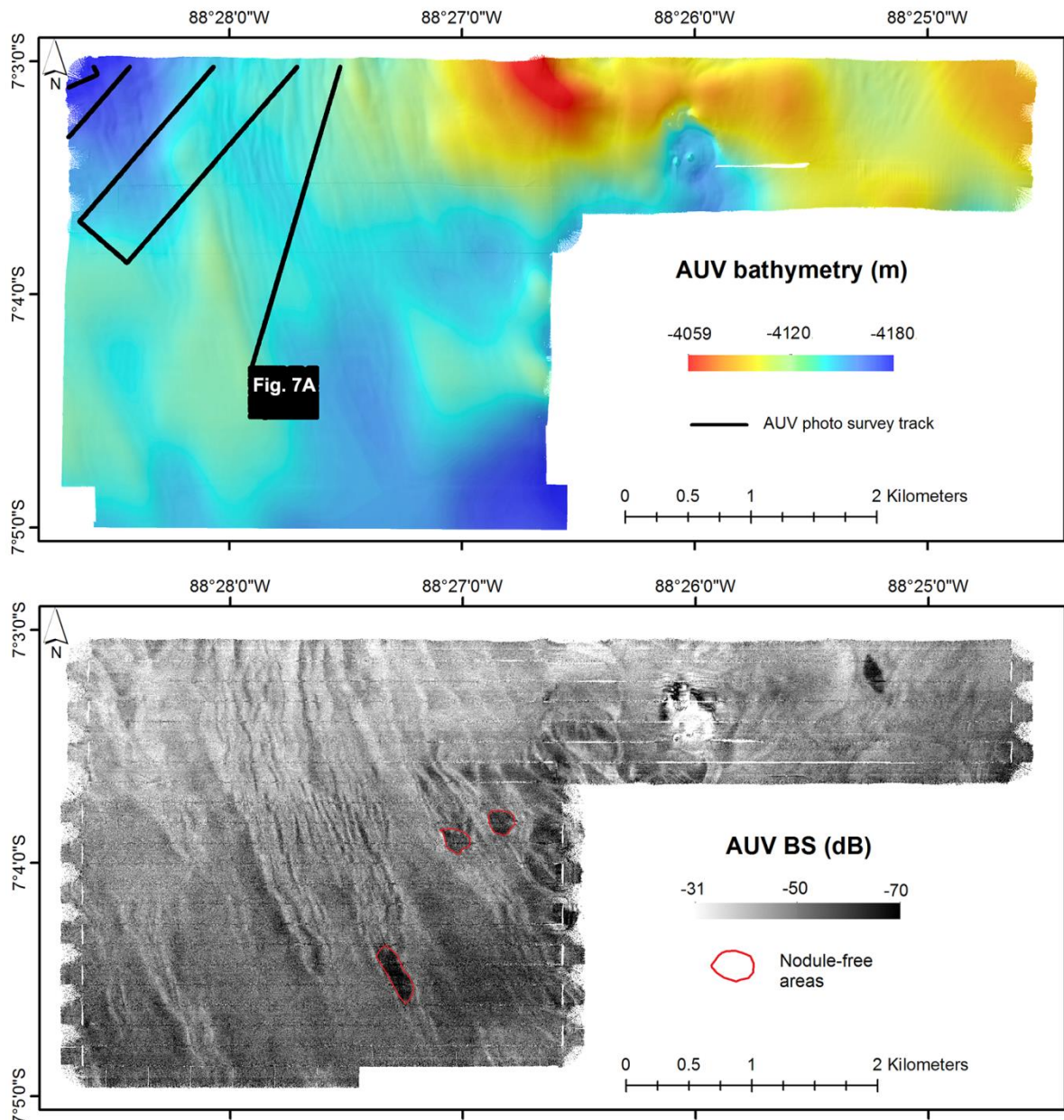
Fig. 2: A) AUV MBES bathymetry with black lines indicating the tracks of the AUV image survey. Closely spaced track lines covering a rectangular area in the lower part of the image correspond to the areas shown in Figures 4A & 7A-D. B) AUV backscatter mosaic. The polygons delineated in red represent nodule-free areas as observed from underwater video data.

763
764
765
766
767
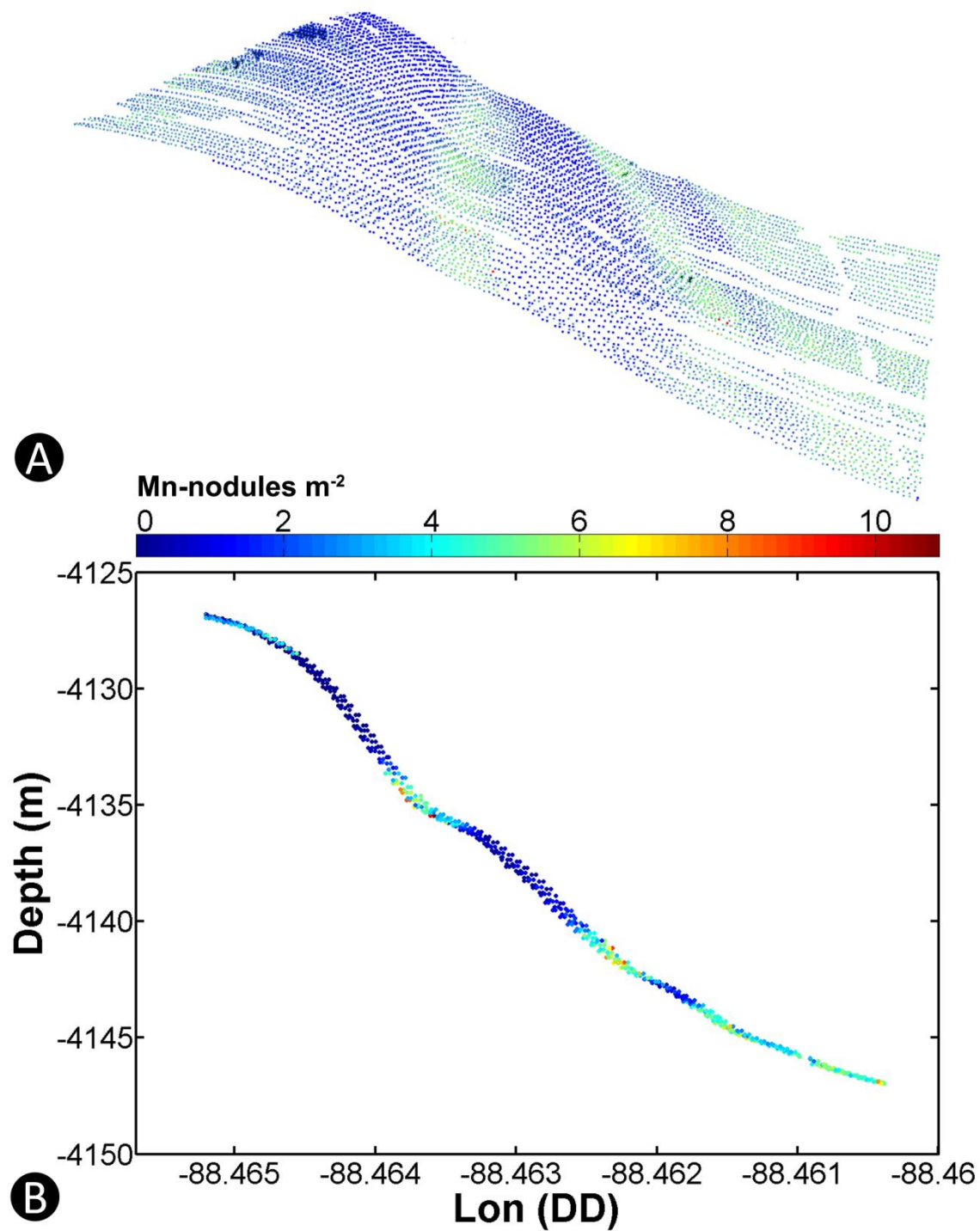
Fig. 4: A) Points with nodule measurements derived from automated nodule detection, draped on AUV bathymetry, showing Mn-nodules per square meter from perspective view, B) Longitudinal section of bathymetric profile from same area highlighting the local scale morpho-bathymetry of Mn-nodule fields.

768
769
770
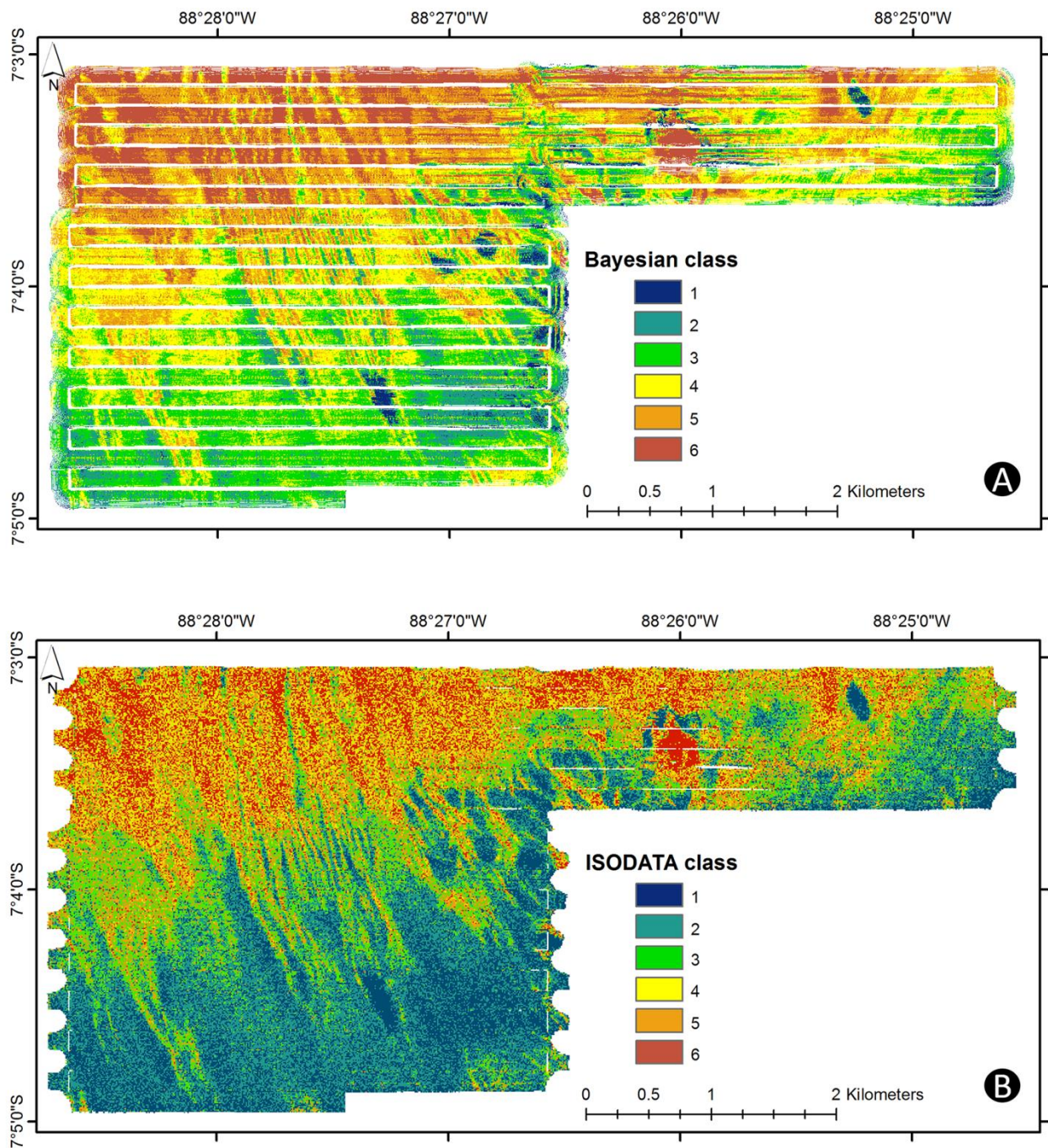
Fig. 5: A) Bayesian classification map based on AUV backscatter beam data, B) ISODATA classification map based on AUV backscatter neighbourhood statistics (mean, mode, 10th Q and 90th Q, see Table 2).

771

772

773

774

775
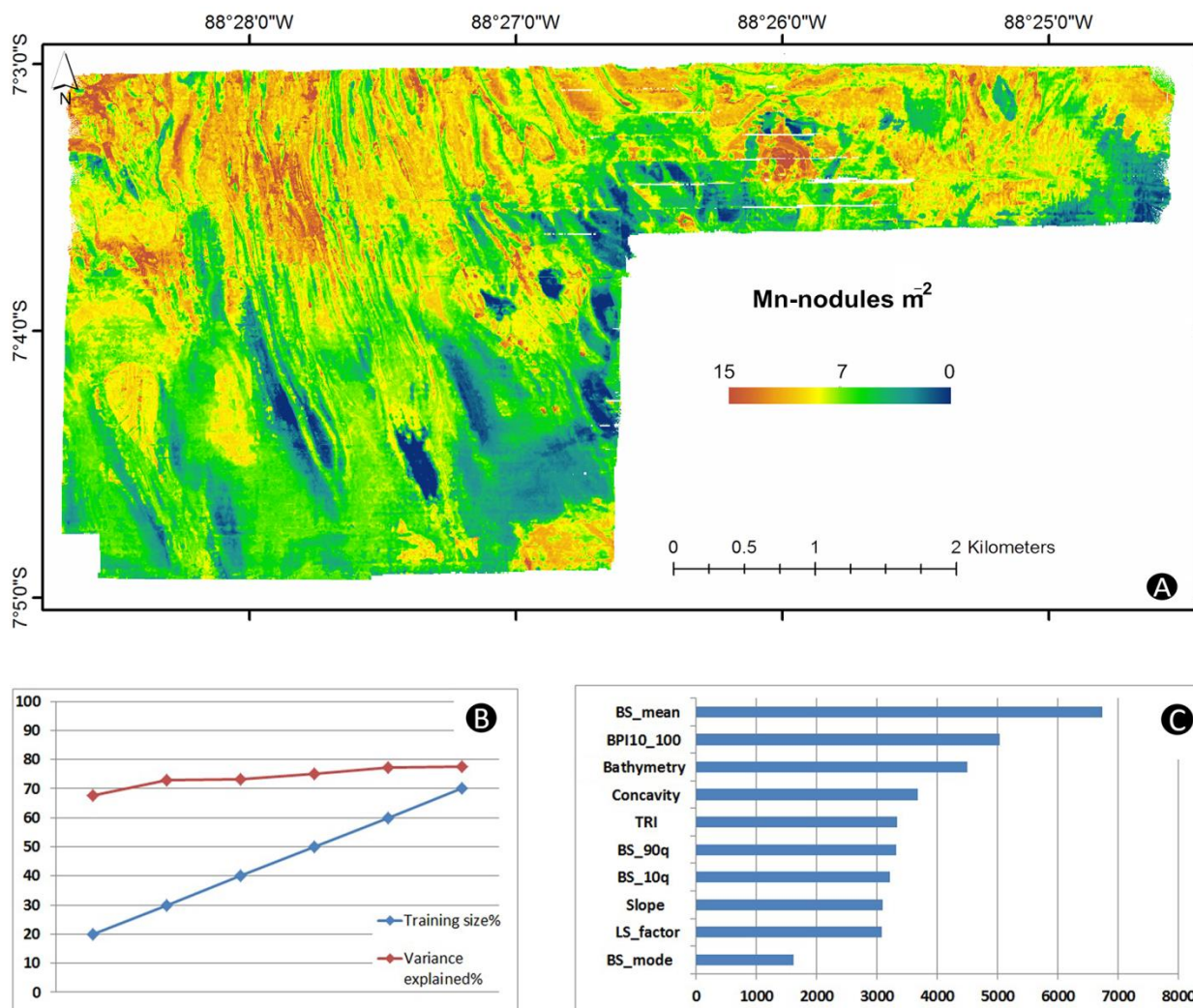
Fig. 6: A) Random forests prediction map of Mn-nodules densities, Sensitivity analysis results: B) Percentage of training sample size and performance of RF model in terms of percentage of variance explained (out-of-bag). C) Importance scores of MBES explanatory variables, based on average percentage increase of mean prediction error from ten model runs.

776
777
778
779
780
781
782
783
784
785
786
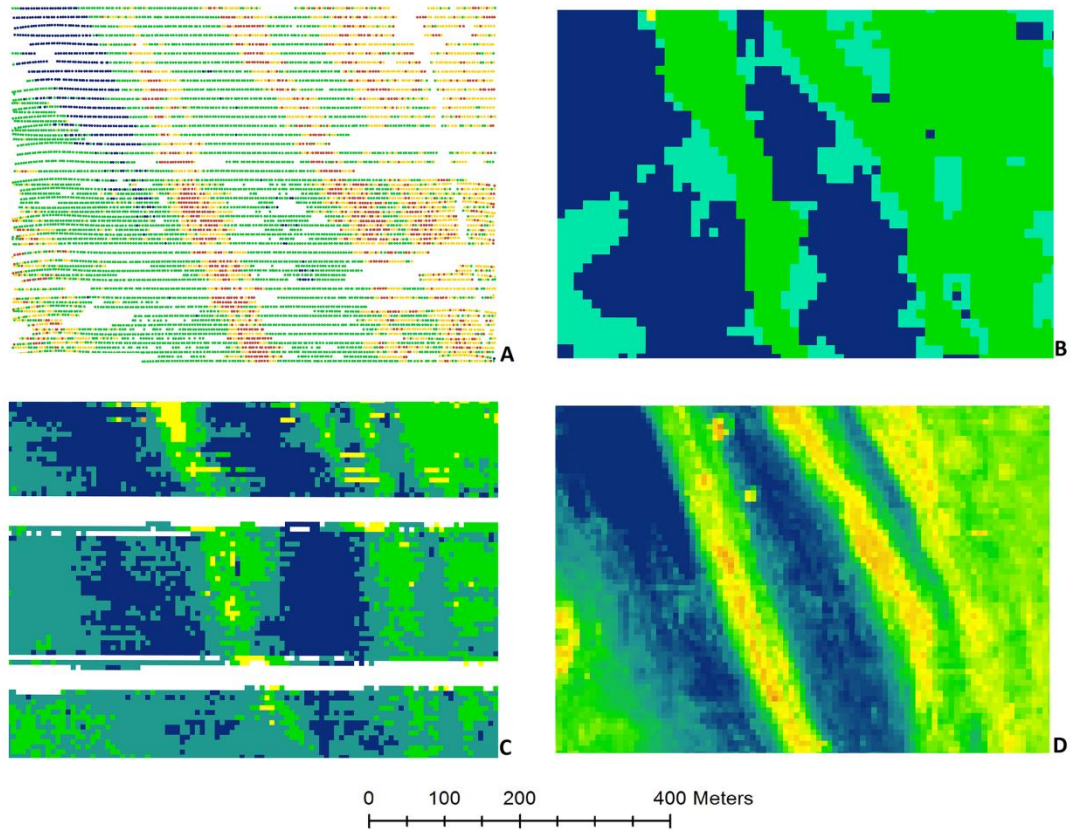
Fig. 7: Inter-comparison of quantitative methods results from the same coverage area (Rectangle made by dense black lines in Fig. 2 A): A) Mn-nodules per image-point (automated nodule-detection from optical images), B) ISODATA classes (10m cell size), C) Bayesian classes (6m cell size), D) RF Mn-nodule density prediction map (6m cell size).

787

26
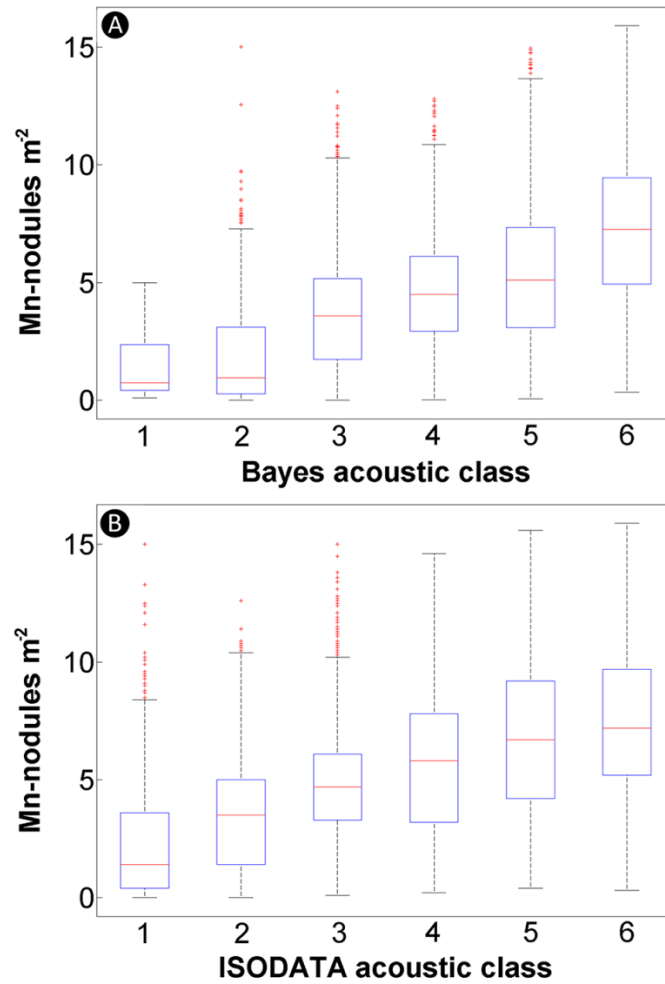
Fig. 8: Box-plots of nodule densities grouped by acoustic class to illustrate the between-class variability. A) Variation of measurements, from samples belonging A) to the same Bayesian classes and B) same ISODATA classes. Blue rectangle bottom and top represent the 25% and 75% percentiles respectively whereas the red line indicates the median value. The whiskers extend to the minimum and maximum value of the samples that are not considered outliers (i.e.: they are no more than ±2.7σ apart). Outliers are marked with red crosses.

788
789
790
791
792
793
794
795
796
797
798
799
800

APPENDIX
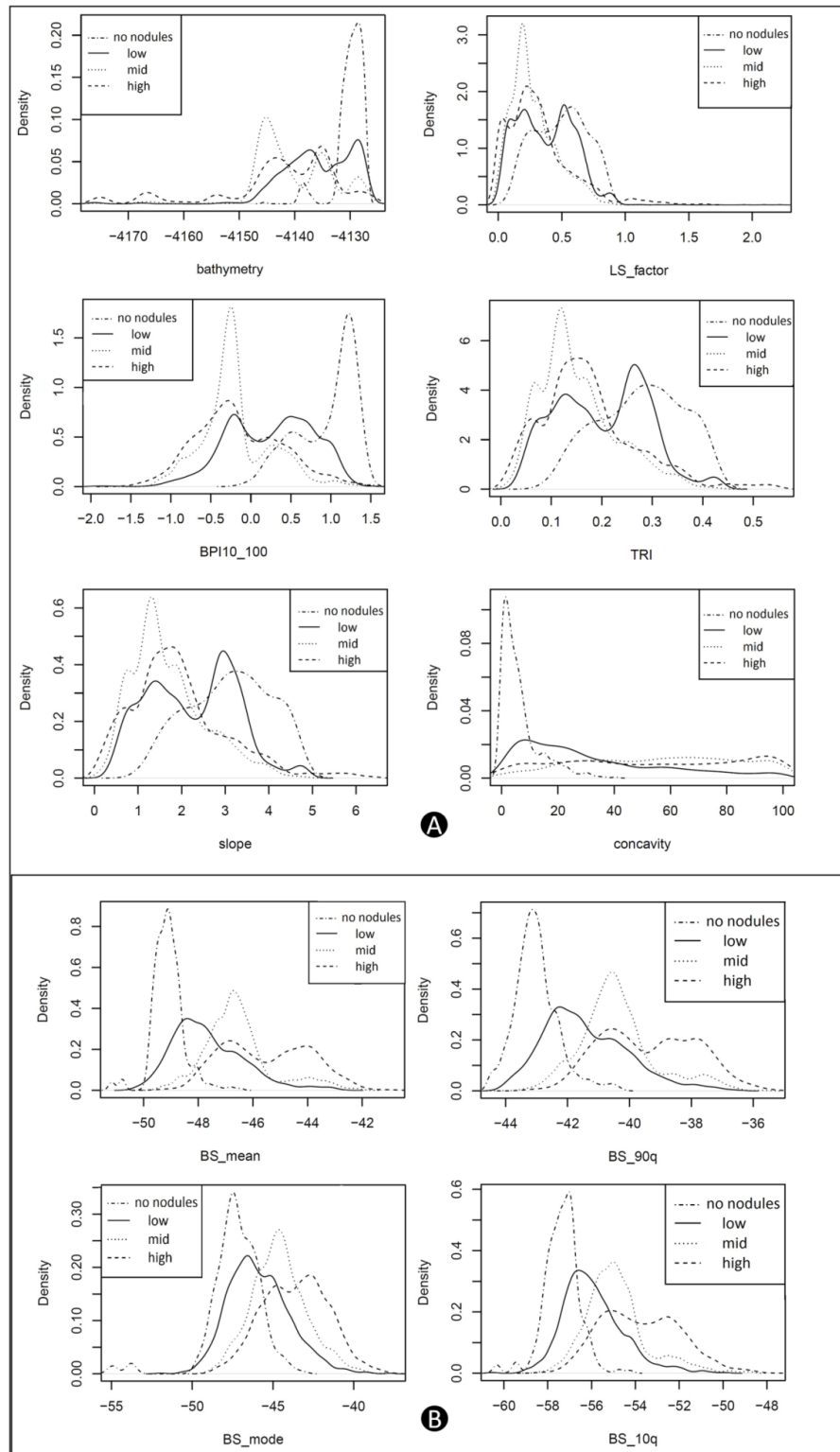
Fig. 3: Data exploration results showing probability density functions for arbitrary classes of nodules per image (<10: no nodules, 10-184: low, 185-270: mid, >270: high) for A) bathymetry and derivatives and B) Backscatter and neighbourhood statistics.

802

Error sources in quantitative Mn-nodule mapping

A few error sources need to be considered when performing seafloor classification and nodule density estimates with optical and acoustic data acquired during multiple AUV deployments.

1) *Noisy backscatter data*: Since the Bayesian approach uses the raw backscatter data, any final classification is susceptible to the effects of noise. Hence, beam incidence angles less than 20 degrees were discarded due to extreme nadir noise effects. The ISODATA classification was based on the backscatter mosaic and its statistics which are also affected mainly by nadir specular noise. It is thus strongly recommended that backscatter data are properly corrected for geometric and sensor-related effects during pre-processing and grids are also filtered/smoothed before the final classification.

2) *AUV navigation*: As exact underwater navigation in 4 km water depth is generally a difficult task, relative misalignments of data from different deployments are very common. Differences in absolute positioning between two deployments can easily amount to 100 m. Thus correlating image based nodule densities from one deployment with backscatter values from another dive might introduce correlation errors that also impact predictability. Although the large scale spatial pattern of classes is well defined, these misalignments can slightly alter the position of class boundaries causing disagreement with the nodule density measurements in places. A correct and verified re-navigation of all AUV-tracks is important for all subsequent analyses. This was done during this study, but slight misalignments remain.

3) *Nodule sediment blanketing*: The effect of Mn-nodules being blanketed by sediment needs to be considered as a source of error here as the individual nodule size and thus the seafloor coverage might be underestimated by automated annotation. Apart from natural sedimentation, the re-deposition of the plume cloud caused by ploughing during the first disturbance experiment (conducted in 1989), has covered certain parts of the nodule field which might lead to a lower nodule densities in those areas. This effect can artificially reduce the correlation between acoustic classes and Mn-nodule densities given that backscatter is not affected by sediment blanketing.